Article

Structural complexity biases vegetation greenness measures

🔵 Check for updates

Yelu Zeng [1,2,13] ✉, **Dalei Hao** [3,13] ✉, **Taejin Park** [4,5,13], **Peng Zhu**[6], **Alfredo Huete** [7], **Ranga Myneni**[8], **Yuri Knyazikhin**[8], **Jianbo Qi**[9], **Ramakrishna R. Nemani**[4,5], **Fa Li** [2], **Jianxi Huang** [1], **Yongyuan Gao** [1], **Baoguo Li**[1], **Fujiang Ji**[2], **Philipp Köhler** [10], **Christian Frankenberg** [11], **Joseph A. Berry** [12] & **Min Chen** [2] ✉

Vegetation 'greenness' characterized by spectral vegetation indices (VIs) is an integrative measure of vegetation leaf abundance, biochemical properties and pigment composition. Surprisingly, satellite observations reveal that several major VIs over the US Corn Belt are higher than those over the Amazon rainforest, despite the forests having a greater leaf area. This contradicting pattern underscores the pressing need to understand the underlying drivers and their impacts to prevent misinterpretations. Here we show that macroscale shadows cast by complex forest structures result in lower greenness measures compared with those cast by structurally simple and homogeneous crops. The shadow-induced contradictory pattern of VIs is inevitable because most Earth-observing satellites do not view the Earth in the solar direction and thus view shadows due to the sun–sensor geometry. The shadow impacts have important implications for the interpretation of VIs and solar-induced chlorophyll fluorescence as measures of global vegetation changes. For instance, a land-conversion process from forests to crops over the Amazon shows notable increases in VIs despite a decrease in leaf area. Our findings highlight the importance of considering shadow impacts to accurately interpret remotely sensed VIs and solar-induced chlorophyll fluorescence for assessing global vegetation and its changes.

Terrestrial vegetation plays important roles in carbon, water and energy exchanges between the land and the atmosphere. Changes in global vegetation structure and function have been quantified as changes in so-called vegetation greenness, an integrative measure of leaf chlorophyll content, leaf area, species composition, and canopy cover and structure. Spectral vegetation indices (VIs) and the green leaf area index (LAI) from Earth-observing satellites are commonly used as proxies of vegetation phenology and provide quantitative, timely and accurate information on the vegetation growing status[1–6]. These VIs are typically calculated as the ratio of surface reflectance

[1]College of Land Science and Technology, China Agricultural University, Beijing, China. [2]Department of Forest and Wildlife Ecology, University of Wisconsin–Madison, Madison, WI, USA. [3]Atmospheric Sciences and Global Change Division, Pacific Northwest National Laboratory, Richland, WA, USA. [4]NASA Ames Research Center, Moffett Field, CA, USA. [5]Bay Area Environmental Research Institute, Moffett Field, CA, USA. [6]Department of Geography and Institute for Climate and Carbon Neutrality, The University of Hong Kong, Hong Kong SAR, China. [7]Faculty of Science, University of Technology Sydney, Sydney, New South Wales, Australia. [8]Department of Earth and Environment, Boston University, Boston, MA, USA. [9]Centre d'Etudes Spatiales de la Biosphere, Toulouse, France. [10]EUMETSAT, Darmstadt, Germany. [11]Jet Propulsion Laboratory, California Institute of Technology, Pasadena, CA, USA. [12]Department of Global Ecology, Carnegie Institution for Science, Stanford, CA, USA. [13]These authors contributed equally: Yelu Zeng, Dalei Hao, Taejin Park. ✉e-mail: zengyelu123@gmail.com; dalei.hao@pnnl.gov; min.chen@wisc.edu

at specific wavelengths due to the contrasting spectral signatures of vegetative and non-vegetative (for example, background substrate and atmosphere) features, at these wavelengths. A greenness index typically contrasts a primary absorption band against a non-absorbing one. The red-versus-near-infrared (NIR) contrast on vegetation is stronger than the red-versus-green contrast and thus is more widely used, although NIR is beyond the visible colour 'green'[3,4]. Example VIs include the widely used ratio-based normalized difference vegetation index (NDVI), the enhanced vegetation index (EVI) and the near-infrared reflectance of vegetation (NIRv), which include the ratio plus a dependence on the absolute value of NIR reflectance[1,7,8]. Their simplicity has enabled various Earth science applications since the 1970s, such as monitoring crop growth status[9,10], detecting vegetation phenophase[7,11–13] and assessing climate change impacts on terrestrial ecosystems[2,4,14,15].

VI-informed greenness is not explicit about the underlying physical mechanisms and can result in important ambiguities, thus misinterpretation. For example, VIs from satellites are typically sensitive to the variation of seasonal sun–sensor geometry and thus have been suggested to be normalized to a nadir view direction and a constant solar zenith angle or at local solar noon[16,17]. This angular normalization is critical because geometry-induced seasonal VI changes can be misinterpreted as ecological signals, leading to controversial debates, for example, seasonality in the Amazon rainforest[11,17,18]. In addition, sensors onboard satellites sample only a small and variable fraction of the total canopy-reflected photons in a certain view direction, and, therefore, there remains a large gap between the satellite-observed signal and the total signal reflected by the canopy. Recent advances in radiative transfer theory bridge such a gap by introducing a new physical parameter, namely, the photon escape probability (f_{esc})[3,19]. The concept of f_{esc} was initially introduced to measure the photon escape probability of solar-induced chlorophyll fluorescence (SIF)[19], and subsequent research[3] has demonstrated that f_{esc} can also be used for characterizing the ratio of canopy-reflected photons (that is, top-of-canopy reflectance) in the visible–NIR region and thus the derived VIs such as NIRv.

The f_{esc} is defined as the ratio of photons escaping from the canopy that are observed by the sensor to the photons intercepted and then reflected or emitted by the canopy. This directly measurable parameter is primarily dependent on the canopy structure and sun–sensor geometry. It can be considered as a physical structural property of vegetation, which could be used as a key metric to diagnose and explain biases between the satellite-received light and the light intercepted and then reflected or emitted by the canopy. The f_{esc} in the NIR band can be approximated by the ratio of NIRv to the fraction of photosynthetically active radiation (FPAR)[19], and is approaching the NIR reflectance or albedo for dense canopies, which means that shaded canopies lead to smaller reflectance or albedo and f_{esc}. The f_{esc} may help answer questions regarding our long-standing view of the global distribution and trends of vegetation greenness, as the typical VIs do not fully take into account the structural complexities of vegetation canopies[20] in their derivations. Different degrees of structural complexity of biomes will lead to varying levels of f_{esc} and result in incomparable spectral greenness measures; that is, the fraction of sensor-measured signal to total signal interacting with the canopy differs[3,19,21]. Thus, the use of VIs would be particularly challenging in explaining patterns across different biomes where canopy structural complexity varies strongly, for example, forests versus croplands.

Meanwhile, the green LAI, as a measure of abundance of green leaves, is also widely used to represent vegetation greenness[4,22]. Remotely sensed LAI is typically retrieved from a comprehensive radiative transfer model that explicitly considers the vegetation structural characteristics, including diverse biome types, shadows and sun–sensor geometry[5,11,22]. So, in contrast to VIs, LAI-based vegetation greenness analyses account for shadows and theoretically do not suffer the impacts of the complex vegetation canopy structure[23]. Given the

theoretical foundation for f_{esc}, we hypothesize that higher structural complexity in forest ecosystems associated with smaller f_{esc} complicates spectral greenness and biases global vegetation greenness relative to the satellite LAI products as the reference and, therefore, may result in inconsistent findings of the variations of vegetation greenness. We combine three independent investigations to test our hypothesis (Methods).

Results and discussion

Contrasting patterns over the Corn Belt and Amazon rainforest

First, we examine the spatial patterns of satellite-derived global VIs (NDVI, EVI and NIRv) and LAI together with f_{esc} in the NIR band (Fig. 1). At the global scale, we find that all VIs derived from the Moderate Resolution Imaging Spectroradiometer (MODIS), except NDVI, exhibit similar spatial patterns during the peak growing season of crops in the Northern Hemisphere summer. Specifically, these VIs show greater values over cropland-dominated regions compared with those over densely forested regions covering most tropical rainforests, although densely forested regions have higher LAIs (Extended Data Fig. 1). This contrasting pattern is most obvious in the Amazon rainforest region and the US Corn Belt during the Northern Hemisphere summer, even though this period corresponds to the relatively dry season in the Amazon, when the rainforest there may not necessarily have the largest LAI values over a year. We focus on these two dense biomes as representatives of the structurally complex forest and uniform cropland, respectively. Over the US Corn Belt, we observe a higher EVI (mean ± s.d., 0.61 ± 0.06) and NIRv (0.33 ± 0.04) compared with those over the Amazon (EVI = 0.55 ± 0.04, NIRv = 0.27 ± 0.02), whereas the rainforest has a higher LAI (5.7 ± 0.6) than the Corn Belt (2.6 ± 0.3; Fig. 1 and Extended Data Fig. 2). As hypothesized, this contrasting pattern of VIs and LAI is strongly associated with f_{esc} in the NIR band; that is, a high LAI with low f_{esc} (0.31 ± 0.03) in the Amazon leads to low VIs, whereas a low LAI with high f_{esc} (0.45 ± 0.04) in the Corn Belt produces a high EVI or NIRv. The responsive degree of VIs (EVI and NIRv) to the LAI theoretically can be an empirical indicator of f_{esc}[19]. For instance, the slope of LAI–EVI over the Corn Belt was at least twice as high as the slope over the Amazon rainforest (Extended Data Fig. 3), implying a lower (or higher) f_{esc} in the Amazon (or Corn Belt). This suggests that the spatial or temporal analysis of VI-based greenness across biomes could be biased because the same VI can correspond to dramatically different amounts of leaves (that is, LAI). To avoid the possible anomaly of VIs and LAI caused by climate extremes in certain years, the yearly data in August in 2001–2019 were evaluated (Extended Data Fig. 4) as a comparison with the long-term average data in Fig. 1. A few more global VI and LAI products, including the MOD13 NDVI and EVI, Geoland (GEOV) LAI and Global LAnd Surface Satellite (GLASS) LAI, were used for the analysis (Methods and Extended Data Fig. 5) as a comparison with the MCD43 NDVI and EVI, and MODIS LAI, in Fig. 1 and the MCD43-based difference vegetation index, the two-band version of the EVI and the newly proposed kernel normalized difference vegetation index[24] in Extended Data Fig. 2. The green–red vegetation index (GRVI)[25] was used as a proxy of canopy pigment pools to evaluate the contrast under the control of similar pigments (Extended Data Fig. 6). A forest region in North America near the Corn Belt with the same season and a similar latitude and sun–sensor geometry was included for the analysis (Extended Data Fig. 7). The observation-based findings are consistent across different LAI data from different algorithms and satellite data (Extended Data Fig. 5), years (Extended Data Fig. 4), regions (Extended Data Fig. 7) and VIs (Extended Data Fig. 2).

Structural complexity biases spectral vegetation greenness

We then use multi-angular satellite observations to examine the role of vegetation structure and associated shadow impacts on the identified discrepancy of VIs over the Amazon rainforest and the Corn Belt (Fig. 2). Two important indicators are used, that is, angular variation
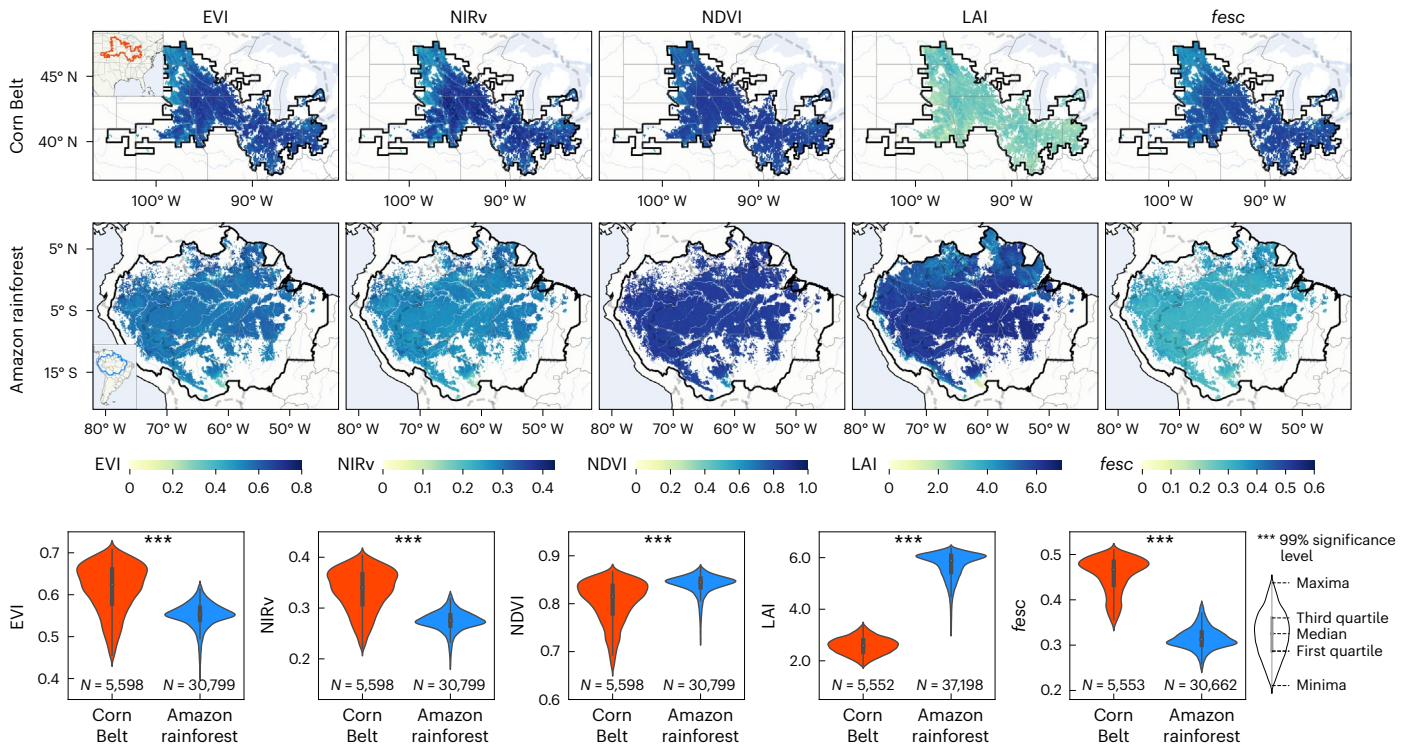
Fig. 1 | Comparisons of VIs, LAI and *fesc* between the US Midwest Corn Belt (43° N and 94° W, 824,871 km²) and the Amazon rainforest (5° S and 62° W, 7,755,160 km²) in August in 2001–2019. The corresponding violin plots display the quartiles and means of the target variables. The MODIS EVI, NIRv and *fesc* were lower over the Amazon rainforest compared with those over the Corn Belt owing to the stronger shadows in view. By contrast, the MODIS LAI was higher in the Amazon rainforest than in the Corn Belt.
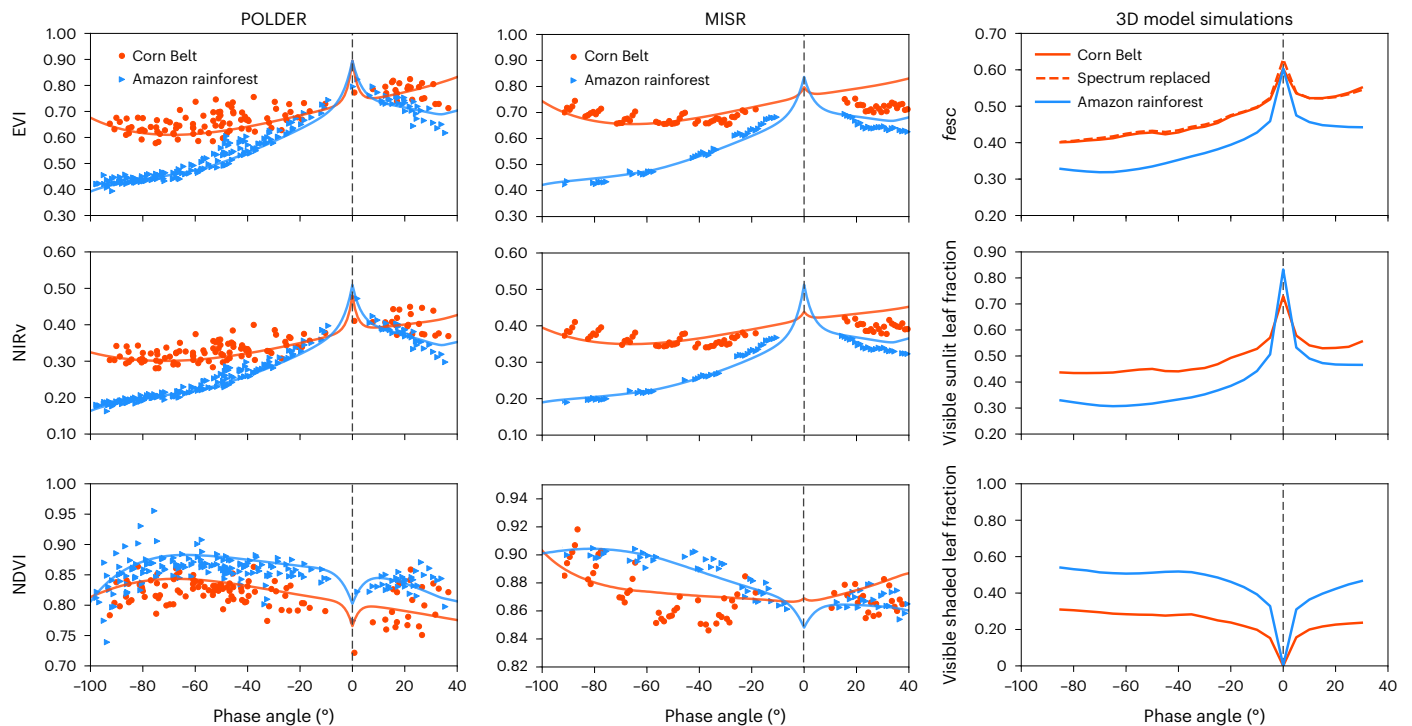

Fig. 2 | POLDER (July–August 2008), MISR (July–August 2017) and 3D ray-tracing model simulated multi-angular observations in summer. The EVI, NIRv, *fesc*, and visible sunlit and shaded leaf fractions of the Corn Belt and Amazon rainforest are similar at the hotspot (phase angle = 0 when the solar and sensor directions coincide), whereas the EVI, NIRv, *fesc* and visible sunlit leaf fraction of the Corn Belt are always much higher than those of the Amazon rainforest at the off-hotspot directions (phase angle ≫ 0, for example, at nadir view, but the solar zenith angle is 45° for the standard Multi-Angle Implementation of Atmospheric Correction surface reflectance product). The phase angle is the angle between the solar and sensor directions. 'Spectrum replaced' represents the simulation of the corn field, and the soil–leaf spectrum was replaced by the spectrum of the Amazon rainforest. The minimal changes after replacing the soil–leaf spectrum suggest the *fesc* was primarily driven by the canopy structure and sun–sensor geometry instead of the leaf optics.
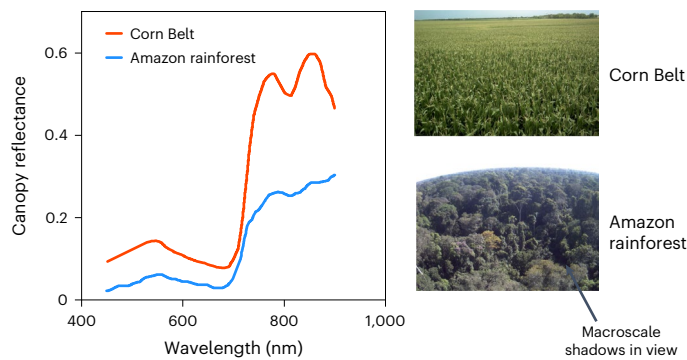
Fig. 3 | An example of the canopy spectrum in summer over the Amazon rainforest and the Corn Belt acquired by the Earth Observing-1 Hyperion sensor. A greater proportion of shadows in the field of view per unit area is observed over the Amazon rainforest than over the Corn Belt in the PhenoCam images (https://phenocam.nau.edu/webcam). The sample spectrum over the Corn Belt was acquired on DOY 210 in 2014, and the spectrum over the Amazon rainforest was acquired on DOY 221 in 2002. The Hyperion images were atmospherically corrected with the available visibility data to convert radiance to surface reflectance. Photo credits: data from ref. 58; images from PhenoCam under a Creative Commons licence CC BY 3.0.

of VIs and hotspot-direction VIs. The angular variation of VIs can be a proxy of canopy structural complexity because a more complex canopy casts more shadows leading to a larger angular variation. The hotspot-direction VIs offer valuable insights into surface vegetation by minimizing shadows in view and maximizing *fesc*, regardless of vegetation type. Note that the hotspot direction is an observing condition when the sun and sensor directions coincide (that is, phase angle $\gamma = 0$). Two multi-angle imaging satellites are used: Polarization and Directionality of the Earth's Reflectances (POLDER) and Multi-angle Imaging SpectroRadiometer (MISR)[26,27]. Both multi-angular observations from POLDER and MISR capture general hotspot angular signatures of VIs, revealing larger angular variations over the Amazon rainforest compared with the Corn Belt in the EVI and NIRv (Fig. 2). For the EVI, the coefficient of variation (defined as the ratio of the standard deviation to the mean) of POLDER (MISR) across the entire angular range was 0.20 (0.16) over the Amazon rainforest, whereas it was only 0.09 (0.06) over the Corn Belt. Similarly, the coefficient of variation of NIRv from POLDER (MISR) was 0.27 (0.22) over the Amazon rainforest, whereas it was only 0.12 (0.07) over the Corn Belt. At the condition of angular normalization we used for the MODIS ($\gamma = 28.8° \pm 2.1°$ for the Corn Belt and $19.4° \pm 6.0°$ for the Amazon rainforest), we detect similar VI patterns observed from the MODIS, that is, a higher EVI and NIRv over the Corn Belt compared with those over the Amazon rainforest. However, this pattern over the two biomes is reversed when the sensors see vegetation canopy at the hotspot direction ($\gamma = 0°$). As the sensor direction deviates from the solar direction (that is, the phase angle increases), there are different change rates for the two biomes: the Amazon rainforest EVI and NIRv on POLDER (MISR) decrease as large as 7.8% (7.3%) and 9.5% (9.3%), respectively, for every 10° increase in phase angle, whereas the Corn Belt EVI and NIRv on POLDER (MISR) decrease only 3.7% (3.4%) and 3.8% (3.7%), respectively. This suggests that VI-based greenness (away from the hotspot direction) could be impacted differently by the structure complexities whereas the impact may be minimized if the VIs are angularly normalized to the hotspot direction. Unlike the EVI and NIRv, the NDVI in the hotspot direction is observed to be lower than those in other directions, whereas there is no obvious NDVI change along the range of phase angles, which is possibly due to the saturation of the NDVI over dense canopies[28] and *fesc* partially cancelling out from the numerator and denominator of the ratio-based VIs but not cancelling out for the NIRv with the additional NIR scalar. We also find no significant

angular variations in POLDER and MISR NDVIs for both biomes, with changes no more than 2.0% observed for every 10° increase of the phase angle (Kolmogorov–Smirnov test: $p < 0.05$). This suggests that the issue of shadow-induced bias affects many commonly used VIs, except that the impact is smaller for some purely ratio-based indices like NDVI.

Finally, we use a state-of-the-art three-dimensional (3D) photon-ray-tracing model (large-scale remote-sensing simulation, LESS)[29] to explicitly quantify the roles of the visible sunlit or shaded leaf fraction in view together with *fesc* (Fig. 2). The vegetation structure parameters and leaf–soil spectrum of the two regions are prepared from the field data, airborne light detection and ranging (LiDAR) measurements and literature review (Supplementary Table 1 and Extended Data Fig. 8)[12,30]. The angular signatures of the VIs over the biomes from the LESS capture vegetation–photon interactions at various sun-sensor geometries and structural complexities of the vegetation canopy (Fig. 2). Our analysis points out that the visible sunlit leaf fraction in view and *fesc* for the two biomes decrease, but their change rates are greater in the Amazon rainforest (10.5% and 7.7% per 10° phase angle) compared with the US Corn Belt (6.6% and 5.1% per 10°), similar to how EVI and NIRv behave. Similarly, the visible shaded leaf fraction in view for the two biomes increases but their change rates are also greater in the Amazon rainforest (8.4% per 10°) compared with those in the Corn Belt (4.7% per 10°). These simulated angular variations conform to the patterns observed in two multi-angle imaging satellites. To mediate impacts of soil–leaf optic characteristics in the two biomes, we repeated the simulation of the corn field by adopting the soil–leaf spectrum of the Amazon rainforest. The simulation of the corn field with the soil–leaf spectrum from the Amazon rainforest reveals minimal changes. Additional sensitivity experiments show that *fesc* in view was primarily driven by the shadowing impacts from the canopy structure and sun–sensor geometry instead of the leaf and soil optical properties (Fig. 2). For most satellites, when the phase angle is larger than 15° or at nadir view, such as in Landsat, the visible sunlit leaf fraction in view and *fesc* for the Corn Belt can be always larger than those for the Amazon rainforest (Fig. 2).

We further conduct both the remote-sensing observations (Extended Data Fig. 7) and 3D model simulation-based sensitivity analyses (Extended Data Fig. 9) for a more systematic and unbiased comparison. First, we control the chlorophyll content, soil background and LAI parameters (Supplementary Table 2) in LESS to evaluate the shadow effect under a possible range of canopy structural and leaf–soil optical properties (Extended Data Fig. 9). The EVI and NIRv under the control of similar LAIs (2.5 or 5) are smaller over forests than over crops, especially when the LAI is relatively large at 5. Second, as the chlorophyll content could potentially impact the VIs in the analysis based on remote-sensing data, we further test the GRVI as a proxy of canopy pigment pools to examine the impacts of the pigments. We add the comparisons under the control of similar GRVIs (such as 0.1–0.15, 0.15–0.20, 0.20–0.25; Extended Data Fig. 6). The results suggest that the MODIS EVI, NIRv and *fesc* under the control of similar GRVIs are smaller over the Amazon rainforest than over the Corn Belt, whereas the MODIS LAI shows the opposite pattern. Lastly, considering that the forest in the Amazon has much larger LAI values than the crops in the Corn Belt, we have compared the Corn Belt and a nearby forest region in North America. These two regions have more similar LAIs and share the same season, similar latitudes and sun–sensor geometry (Extended Data Fig. 7). Extended Data Fig. 7d suggests that the MODIS EVI under the control of similar LAIs (2.0–2.5, 2.5–3.0, 3.0–3.5) and GRVIs (0.1–0.15, 0.15–0.20, 0.20–0.25) is smaller over the nearby forest region in North America than over the Corn Belt. After we compare the VIs under the control of similar LAIs and canopy pigment content, the results in the comparison of VIs between forest and cropland draw a solid conclusion that the observed VIs are strongly affected by the shadow effect.

Fig. 4 | The opposite trend of LAI and EVI time series in land-cover transition.
a, The opposite trend of the annual maximum MODIS LAI (insignificant or significant decrease) and EVI (significant increase, $p < 0.05$) time series in 2001–2019 at eight deforestation locations (Extended Data Fig. 10) with the land-cover change from forest to crops within 2005–2015 over the Amazon rainforest. The error bars represent the standard error of the mean for each annual maximum EVI or LAI time series. **b**, The opposite trend of the annual maximum MODIS LAI (insignificant decrease, $p > 0.05$) and EVI (significant increase, $p < 0.05$) time series for all the deforestation pixels from forest to crops (within 2005–2015)

over the whole Amazon rainforest. Note that crops can have a higher EVI than forests at the same LAI owing to less impact of shadows. The LAI or EVI data were normalized using the equation (LAI or EVI − mean)/mean. The dots mark the mean, and the error bars represent 95% confidence intervals. These intervals were calculated by conducting a two-sided t-test on the sample data, with no adjustments made for multiple comparisons. The trendlines were fitted with ordinary least-squares regression. The translucent region around the trendlines represents the 95% confidence interval, estimated using the bootstrap method.

The impact of macroscale shadows due to forest canopy structure (Fig. 3) has been ignored in conventional VI-based greenness studies[4,17]. In this study, we find that even if the satellite observations are normalized to nadir viewing geometry and at local solar noon following the common recommendation[17], there still can be varying proportions of macroscale shadows in view for forests and crops with different complexities of vegetation structures. These shadows play a first-order role in further complicating the remote-sensing signals. The observed shadow impact also applies to remotely sensed SIF because SIF and optical photons at the same wavelengths undergo similar radiative transfer processes and share a common *fesc*[19,31]. Our supplemental analysis of SIF and PAR-normalized SIF shows a consistent global pattern with those of EVI and NIRv, displaying a higher SIF over the Corn Belt compared with the Amazon rainforest, but this pattern is opposite to that of LAI (Extended Data Fig. 2).

Spectral greenness bias in land-cover transition

We have shown that shadows driven by complex vegetation structures and observing geometry conditions can bias the vegetation greenness derived from satellite spectral VIs, especially over the Amazon rainforest. The consequences of these findings extend far beyond the technical interpretation of satellite data. First, the stronger negative greenness bias observed by satellite VIs for forests than for crops can lead to unexpected biases in quantifying and interpreting ecological processes, especially regarding their spatial patterns. More importantly, satellite VIs may become more difficult to interpret when abrupt land conversion from forest to crops occurs, for example, deforestation and crop expansion[10,32]. Our analysis of the MODIS EVI and LAI over Amazon forests experiencing a recent land conversion from forest to crops reveals divergent trends in the EVI and LAI at site (see the eight randomly selected sites in Fig. 4a and Extended Data Fig. 10) and regional scale (EVI = 1.69% per year, LAI = −0.24% per year; Fig. 4b) with the relative variation (divided by the multi-year mean). For post-disturbance (fire, insect and so on) recovery, VIs may recover much faster as simpler structures replace complex structures after large disturbances.

Implications for ecological studies

The shadows driven by a complex vegetation structure can decrease the surface reflectance and albedo (Fig. 3), which can reconcile the seemingly contradictory conclusions about the change of land surface albedo due to Earth greening across biomes. Surface albedo has been considered to decrease over greener crops and grassland without strong shadowing effects[33,34], whereas an unexpected increase of albedo is reported in greener forests because of the decreasing dark shadows and increasing bright sunlit canopy coverage[33,35,36]. For short and sparse canopies, the canopy coverage and the leaf–soil spectrum contrast are the main impact factors of the greening–albedo changes, whereas for tall and dense canopies with less soil background impacts, the shadows driven by a complex structure are another important factor that determines the greening–albedo trends. The impact of shadows may become another layer of uncertainty in several downstream applications including canopy nitrogen estimations (Fig. 4 in ref. 37), highlighting the need to consider biome-specific calibrations in accounting for varying canopy structures.

Meanwhile, a complex vegetation structure with stronger shadows can also increase the photon multiple scattering and re-absorption within the canopy. This, in turn, enhances photon capture capability and reduces the impact of pigment pools on achieving the same level of light capture efficiency. Extended Data Fig. 7d suggests that an increase in GRVI in the forest region does not lead to many changes in EVI. However, in the cropland region, an increase in GRVI is accompanied with an increase in EVI. As EVI used to be considered as a proxy of potential photosynthetic capacity[38,39], this observation suggests that, even with the same LAI, there can be variations in the potential photosynthetic capacity. The increase in pigment pools, which is associated with changes in greenness, has a greater impact on crops than forests for vegetation photosynthesis. Recognizing and minimizing the impact of structural complexity on greenness measures also help improve the estimation of large-scale plant photosynthesis (that is, gross primary production) through satellite remote sensing.

In addition, VIs are widely used as a proxy for FPAR which is a critical component of remote-sensing-based models of terrestrial carbon (for example, gross primary productivity)[40–42] and water (for example, evapotranspiration)[43–45] cycles. As shown in our study, EVI and NIRv are 11.5% and 21.8% higher in terms of the mean value in the Corn Belt than in the Amazon rainforest, whereas FPAR is 14.5% lower (Fig. 1 and Extended Data Fig. 2). Therefore, it is unlikely that there exists a universal VI–FPAR relationship across different biomes (Extended Data Fig. 3a), which brings an additional challenge in parameterizing global remote-sensing-based carbon and water models. Although the NDVI is less impacted by shadows than many other VIs, such as the difference vegetation index and NIRv, the slope of the NDVI–FPAR relationship still varies owing to different soil backgrounds and the saturation of NDVI over dense canopies. To minimize the shadowing effect, it is more ideal to use the surface reflectance at the hotspot direction, which is often not directly measured by most satellite missions but possible to infer from kernel-driven bidirectional reflectance models.

Conclusion

Because nearly all the satellite sensors do not view the Earth in the hotspot directions and thus macroscale shadows in view are inevitable, the direct use of the EVI or the NIRv to indicate vegetation greenness can be biased, especially for structurally complex forests. This leads to spatial biases of global vegetation greenness from crops to forests with different complexities of vegetation structure. Considering that cropland expansion is being driven by increasing food production demand, omitting the complexity of vegetation structure might result in greater uncertainty in assessing vegetation changes and growth trends, hindering the accurate quantification of regional and global carbon budgets. Our results highlight such biases and limitations of the widely used VI-based remote-sensing greenness over past decades. However, it is important to clarify that shadows are a real component of vegetation canopies and the shaded cohort usually contributes a large portion of the whole vegetation canopy carbon, water and energy budget[46]. Therefore, satellite products do not necessarily need to be corrected for shadows in many applications, but to minimize the ambiguities in global vegetation greenness with spatio-temporal biome changes, it is beneficial to correct satellite-observed VIs to the hotspot directions[47].

Methods

Datasets and processing

MODIS surface reflectance, VIs and LAI products. We used the daily MODIS MCD43A4 V6.1 Nadir Bidirectional Reflectance Distribution Function–Adjusted Reflectance[16], the 8 day MOD15A2H V6.1 combined LAI and FPAR[48], and the 16 day MOD13A2 V6.1 EVI and NDVI products, and the yearly MCD12Q1 V6.1 Land Cover Type datasets[49]. All MODIS datasets from 2001 to 2019 with 500 m spatial resolution were obtained from the Google Earth Engine platform[50]. We used only the snow-free MODIS Nadir Bidirectional Reflectance Distribution Function– Adjusted Reflectance and other data with good quality assurance and quality control flags. The GEOV LAI product was acquired at https://land.copernicus.eu/global/products/lai, and the GLASS LAI product was acquired at http://www.glass.umd.edu/LAI/MODIS/0.1D/. We used the International Geosphere–Biosphere Programme classification layer in the MCD12Q1 data to calculate the proportions of each land-cover type within a given pixel. The data were aggregated to monthly temporally and 0.1° spatially. For our analysis, we excluded all pixels in which non-vegetation types (such as snow and ice, water,

barren land and urban areas) comprised more than 50% of the total area. In addition, we analysed only homogeneous pixels composed of more than 80% forest or crops within vegetated areas.

TROPOMI SIF and EPIC PAR. We used the TROPOspheric Monitoring Instrument (TROPOMI) far-red daily SIF dataset with a spatial resolution of 7 km × 3.5 km at nadir[51] from ftp://fluo.gps.caltech.edu/data/tropomi and the Deep Space Climate Observatory Earth Polychromatic Imaging Camera (EPIC)-derived daily photosynthetically active radiation (PAR) data with 0.1° × 0.1° spatial resolution[52,53]. The SIF normalized by PAR was calculated and compared with VIs. We used the time period from March 2018 to February 2019 to be consistent with the TROPOMI SIF dataset, which started in March 2018.

POLDER and MISR multi-angular surface reflectance. This study utilized multi-angular observations of surface reflectance from POLDER and MISR during the summer season over the Corn Belt and the Amazon rainforest. The POLDER observations were obtained between July and August 2008, with a spatial resolution of approximately 6.2 km (ref. 26). The MISR observations were collected between July and August 2017, with a spatial resolution of 1.1 km and a temporal resolution of 9 days[11,54].

Earth Observing-1 Hyperion-based canopy spectrum. Two Earth Observing-1 Hyperion images acquired over the Amazon rainforest and the Corn Belt in summer were used in this study. The Hyperion image over the Corn Belt was acquired on day of year (DOY) 210 in 2014, and the Hyperion image over the Amazon rainforest was acquired on DOY 221 in 2002. The Hyperion images were atmospherically corrected with the available visibility data to convert radiance to surface reflectance[55]. The spectrum <500 nm over the Corn Belt was extrapolated owing to the imperfect atmospheric correction of the Hyperion data at shorter wavelengths.

LiDAR dataset and 3D ray-tracing model simulations. The point cloud data were collected during LiDAR surveys over a forest research site (54.99° E, 3.37° S) at the Amazon rainforest in Brazil in 2018[30]. The LiDAR data were collected to characterize the canopy profile and leaf area density, which were used to drive the 3D ray-tracing model simulations. In this study, the LiDAR data of a 100 m × 100 m area were extracted and simulated, and this dataset was available through the Oak Ridge National Laboratory Distributed Active Archive Center at https://daac.ornl.gov/cgi-bin/dsviewer.pl?ds_id=1644. The 3D radiative transfer simulation framework, LESS (large-scale remote-sensing data and image simulation framework over heterogeneous 3D scenes), was used in this study to incorporate the soil–leaf–canopy structure and optical properties[29]. Typical parameters of the row-planted corn field were used in the comparative LESS-based simulations[9]. The 3D LESS model can simulate the multi-angular surface reflectance and visible sunlit and shaded leaf fractions in view. The corresponding multi-angular VIs and f_{esc} were calculated based on the surface reflectance and FPAR. To avoid the potential impact of soil–leaf optics and isolate the impact of the canopy structure and sun–sensor geometry, we added a comparative simulation of the corn field with the soil–leaf spectrum replaced by the spectrum of the Amazon rainforest.

Statistical methods
First, we examine spatial patterns of spectral VIs (EVI, NDVI and NIRv) and the LAI from MODIS. The LAI, defined as one half of the total leaf surface area per unit ground area, is also related to vegetation greenness and, more importantly, can serve as the reference to different VI-based greenness owing to its clear physical interpretation. Second, we use multi-angular satellite VI observations at different sun–sensor geometries with different macroscale shadows in view. Third, for mechanistic understanding, we use a 3D photon-ray-tracing model to evaluate the impact of macroscale shadows in view with vegetation structures reconstructed using airborne LiDAR data to more directly quantify what is observed by the sensor that leads to the biases.

We mainly focus on the US Corn Belt and the Amazon rainforest, as they are representative landscapes with relatively homogeneous (Corn Belt) and complex (Amazon rainforest) canopy structures, and are crucially important regions for global agricultural production, the terrestrial carbon cycle and biodiversity conservation. To ensure a fair comparison between forest pixels in the Amazon and cropland pixels in the US Corn Belt, we analysed only homogeneous pixels composed of more than 80% forest or crop. Our analyses excluded non-forest regions, such as savannah in the eastern part of the Amazon and grassland in the southern part of the Amazon, as identified by the MCD12 land-cover product (Fig. 1). We also have conducted a comparison between the cropland in the Corn Belt and a nearby forest region in North America with the same season and similar latitude and sun–sensor geometry (Extended Data Fig. 7).

To make the comparison more reliable and systematic, we have conducted both remote-sensing observation and 3D model simulation-based sensitivity analyses. In the simulation-based analysis, we control the chlorophyll content, soil background and LAI parameters in Supplementary Table 2, and the corresponding results at different levels of LAI are shown in Extended Data Fig. 9. In the analysis based on remote-sensing data, we further test GRVI as a proxy of canopy pigment pools and conduct the comparisons under the control of similar LAIs (2.0–2.5, 2.5–3.0, 3.0–3.5) and GRVIs (0.1–0.15, 0.15–0.20, 0.20–0.25) as shown in Extended Data Fig. 7d.

To shed light on how vegetation structure biases the interpretation of temporal vegetation greenness changes, we further evaluated the temporal changes of the MODIS EVI and LAI at Amazonian regions where rapid land-cover transition occurred from rainforest to crops in 2001–2019, as identified by the MCD12 land-cover product.

Reporting summary
Further information on research design is available in the Nature Portfolio Reporting Summary linked to this article.

Data availability
The data are available through figshare[56] at https://doi.org/10.6084/m9.figshare.23677407.v1.

Code availability
The source code is available through figshare[57] at https://doi.org/10.6084/m9.figshare.23677260.v1.

References
1. Tucker, C. J. Red and photographic infrared linear combinations for monitoring vegetation. *Remote Sens. Environ.* **8**, 127–150 (1979).
2. Myneni, R. B., Keeling, C., Tucker, C. J., Asrar, G. & Nemani, R. R. Increased plant growth in the northern high latitudes from 1981 to 1991. *Nature* **386**, 698–702 (1997).
3. Zeng, Y. et al. Optical vegetation indices for monitoring terrestrial ecosystems globally. *Nat. Rev. Earth Environ.* **3**, 477–493 (2022).
4. Piao, S. et al. Characteristics, drivers and feedbacks of global greening. *Nat. Rev. Earth Environ.* **1**, 14–27 (2020).
5. Chen, J. M. et al. Vegetation structural change since 1981 significantly enhanced the terrestrial carbon sink. *Nat. Commun.* **10**, 4259 (2019).
6. Zhang, H. et al. A novel red-edge spectral index for retrieving the leaf chlorophyll content. *Methods Ecol. Evol.* **13**, 2771–2787 (2022).
7. Huete, A. et al. Overview of the radiometric and biophysical performance of the MODIS vegetation indices. *Remote Sens. Environ.* **83**, 195–213 (2002).
8. Badgley, G., Field, C. B. & Berry, J. A. Canopy near-infrared reflectance and terrestrial photosynthesis. *Sci. Adv.* **3**, e1602244 (2017).

9. Kimm, H. et al. Deriving high-spatiotemporal-resolution leaf area index for agroecosystems in the US Corn Belt using Planet Labs CubeSat and STAIR fusion data. *Remote Sens. Environ.* **239**, 111615 (2020).

10. Maeda, E. E. et al. Large-scale commodity agriculture exacerbates the climatic impacts of Amazonian deforestation. *Proc. Natl Acad. Sci. USA* **118**, e2023787118 (2021).

11. Bi, J. et al. Sunlight mediated seasonality in canopy structure and photosynthetic activity of Amazonian rainforests. *Environ. Res. Lett.* **10**, 064014 (2015).

12. Wu, J. et al. Biological processes dominate seasonality of remotely sensed canopy greenness in an Amazon evergreen forest. *New Phytol.* **217**, 1507–1520 (2018).

13. Hashimoto, H. et al. New generation geostationary satellite observations support seasonality in greenness of the Amazon evergreen forests. *Nat. Commun.* **12**, 684 (2021).

14. Zhang, Y. et al. A global moderate resolution dataset of gross primary production of vegetation for 2000–2016. *Sci. Data* **4**, 170165 (2017).

15. Park, T. et al. Changes in growing season duration and productivity of northern vegetation inferred from long-term remote sensing data. *Environ. Res. Lett.* **11**, 084001 (2016).

16. Schaaf, C. B. et al. First operational BRDF, albedo nadir reflectance products from MODIS. *Remote Sens. Environ.* **83**, 135–148 (2002).

17. Morton, D. C. et al. Amazon forests maintain consistent canopy structure and greenness during the dry season. *Nature* **506**, 221–224 (2014).

18. Saleska, S. R. et al. Dry-season greening of Amazon forests. *Nature* **531**, E4–E5 (2016).

19. Zeng, Y. et al. A practical approach for estimating the escape ratio of near-infrared solar-induced chlorophyll fluorescence. *Remote Sens. Environ.* **232**, 111209 (2019).

20. Myers-Smith, I. H. et al. Complexity revealed in the greening of the Arctic. *Nat. Clim. Change* **10**, 106–117 (2020).

21. Rautiainen, M. & Stenberg, P. Application of photon recollision probability in coniferous canopy reflectance simulations. *Remote Sens. Environ.* **96**, 98–107 (2005).

22. Chen, C. et al. China and India lead in greening of the world through land-use management. *Nat. Sustain.* **2**, 122–129 (2019).

23. Parker, G. G., Fitzjarrald, D. R. & Sampaio, I. C. G. Consequences of environmental heterogeneity for the photosynthetic light environment of a tropical forest. *Agric. For. Meteorol.* **278**, 107661 (2019).

24. Camps-Valls, G. et al. A unified vegetation index for quantifying the terrestrial biosphere. *Sci. Adv.* **7**, eabc7447 (2021).

25. Yin, G., Verger, A., Descals, A., Filella, I. & Peñuelas, J. A broadband green–red vegetation index for monitoring gross primary production phenology. *J. Remote Sens.* **2022**, 9764982 (2022).

26. Breon, F.-M. & Maignan, F. A BRDF–BPDF database for the analysis of Earth target reflectances. *Earth Syst. Sci. Data* **9**, 31–45 (2017).

27. Diner, D. J. et al. Multi-angle Imaging SpectroRadiometer (MISR) instrument description and experiment overview. *IEEE Trans. Geosci. Remote Sens.* **36**, 1072–1087 (1998).

28. Kaufmann, R. K. et al. Effect of orbital drift and sensor changes on the time series of AVHRR vegetation index data. *IEEE Trans. Geosci. Remote Sens.* **38**, 2584–2597 (2000).

29. Qi, J. et al. LESS: LargE-Scale remote sensing data and image simulation framework over heterogeneous 3D scenes. *Remote Sens. Environ.* **221**, 695–706 (2019).

30. Dos-Santos, M., Keller, M. & Morton, D. *LiDAR Surveys Over Selected Forest Research Sites, Brazilian Amazon, 2008–2018* (ORNL DAAC, 2019); https://doi.org/10.3334/ORNLDAAC/1644

31. Köhler, P., Guanter, L., Kobayashi, H., Walther, S. & Yang, W. Assessing the potential of sun-induced fluorescence and the canopy scattering coefficient to track large-scale vegetation dynamics in Amazon forests. *Remote Sens. Environ.* **204**, 769–785 (2018).

32. Vancutsem, C. et al. Long-term (1990–2019) monitoring of forest cover changes in the humid tropics. *Sci. Adv.* **7**, eabe1603 (2021).

33. Abera, T. A., Heiskanen, J., Pellikka, P., Rautiainen, M. & Maeda, E. E. Clarifying the role of radiative mechanisms in the spatio-temporal changes of land surface temperature across the Horn of Africa. *Remote Sens. Environ.* **221**, 210–224 (2019).

34. Zheng, L. et al. Spatial, temporal, and spectral variations in albedo due to vegetation changes in China's grasslands. *ISPRS J. Photogramm. Remote Sens.* **152**, 1–12 (2019).

35. Alibakhshi, S., Naimi, B., Hovi, A., Crowther, T. W. & Rautiainen, M. Quantitative analysis of the links between forest structure and land surface albedo on a global scale. *Remote Sens. Environ.* **246**, 111854 (2020).

36. Yan, H. et al. Forest greening increases land surface albedo during the main growing period between 2002 and 2019 in China. *J. Geophys. Res. Atmos.* **126**, e2020JD033582 (2021).

37. Ollinger, S. V. et al. Canopy nitrogen, carbon assimilation, and albedo in temperate and boreal forests: functional relations and potential climate feedbacks. *Proc. Natl Acad. Sci. USA* **105**, 19336–19341 (2008).

38. Zhang, Y. et al. Spatio-temporal convergence of maximum daily light-use efficiency based on radiation absorption by canopy chlorophyll. *Geophys. Res. Lett.* **45**, 3508–3519 (2018).

39. Lin, S. et al. Multi-site assessment of the potential of fine resolution red-edge vegetation indices for estimating gross primary production. *Int. J. Appl. Earth Obs. Geoinf.* **113**, 102978 (2022).

40. Xiao, X. et al. Satellite-based modeling of gross primary production in an evergreen needleleaf forest. *Remote Sens. Environ.* **89**, 519–534 (2004).

41. Joiner, J. et al. Estimation of terrestrial global gross primary production (GPP) with satellite data-driven models and eddy covariance flux data. *Remote Sens.* **10**, 1346 (2018).

42. Badgley, G., Anderegg, L. D., Berry, J. A. & Field, C. B. Terrestrial gross primary production: using NIRV to scale from site to globe. *Glob. Change Biol.* **25**, 3731–3740 (2019).

43. Neale, C. M., Gonzalez-Dugo, M. P., Serrano-Perez, A., Campos, I. & Mateos, L. Cotton canopy reflectance under variable solar zenith angles: implications of use in evapotranspiration models. *Hydrol. Process.* **35**, e14162 (2021).

44. Yebra, M., Van Dijk, A., Leuning, R., Huete, A. & Guerschman, J. P. Evaluation of optical remote sensing to estimate actual evapotranspiration and canopy conductance. *Remote Sens. Environ.* **129**, 250–261 (2013).

45. Chen, J. M. & Liu, J. Evolution of evapotranspiration models using thermal and shortwave remote sensing data. *Remote Sens. Environ.* **237**, 111594 (2020).

46. Chen, M. & Zhuang, Q. Evaluating aerosol direct radiative effects on global terrestrial ecosystem carbon dynamics from 2003 to 2010. *Tellus B* **66**, 21808 (2014).

47. Marshak, A. et al. Earth observations from DSCOVR/EPIC instrument. *Bull. Am. Meteorol. Soc.* **99**, 1829–1850 (2018).

48. Myneni, R. et al. Global products of vegetation leaf area and fraction absorbed PAR from year one of MODIS data. *Remote Sens. Environ.* **83**, 214–231 (2002).

49. Friedl, M. A. et al. Global land cover mapping from MODIS: algorithms and early results. *Remote Sens. Environ.* **83**, 287–302 (2002).

50. Gorelick, N. et al. Google Earth Engine: planetary-scale geospatial analysis for everyone. *Remote Sens. Environ.* **202**, 18–27 (2017).

51. Köhler, P. et al. Global retrievals of solar-induced chlorophyll fluorescence with TROPOMI: first results and intersensor

comparison to OCO-2. *Geophys. Res. Lett.* **45**, 10,456–10,463 (2018).

52. Hao, D. et al. Estimating hourly land surface downward shortwave and photosynthetically active radiation from DSCOVR/ EPIC observations. *Remote Sens. Environ.* **232**, 111320 (2019).

53. Hao, D. et al. DSCOVR/EPIC-derived global hourly and daily downward shortwave and photosynthetically active radiation data at 0.1°× 0.1° resolution. *Earth Syst. Sci. Data* **12**, 2209–2221 (2020).

54. Ni, X. et al. Vegetation angular signatures of equatorial forests from DSCOVR EPIC and Terra MISR observations. *Front. Remote Sens.* **2**, 766805 (2021).

55. Aneece, I. P. et al. in *Fundamentals, Sensor Systems, Spectral Libraries, and Data Mining for Vegetation* (eds Thenkabail P. S. et al.) 251–272 (CRC Press, 2018).

56. Zeng, Y. The data for the NEE paper: structural complexity biases vegetation greenness measures. *figshare* https://doi.org/10.6084/ m9.figshare.23677407.v1 (2023).

57. Zeng, Y. The code for the NEE paper: structural complexity biases vegetation greenness measures. *figshare* https://doi.org/10.6084/ m9.figshare.23677260.v1 (2023).

58. Seyednasrollah, B. et al. Tracking vegetation phenology across diverse biomes using Version 2.0 of the PhenoCam Dataset. *Sci. Data* https://doi.org/10.1038/s41597-019-0229-9 (2019).

Acknowledgements

Author contributions

Competing interests

The authors declare no competing interests.

Additional information

Extended data is available for this paper at https://doi.org/10.1038/ s41559-023-02187-6.

Supplementary information The online version contains supplementary material available at https://doi.org/10.1038/s41559- 023-02187-6.

Correspondence and requests for materials should be addressed to Yelu Zeng, Dalei Hao or Min Chen.
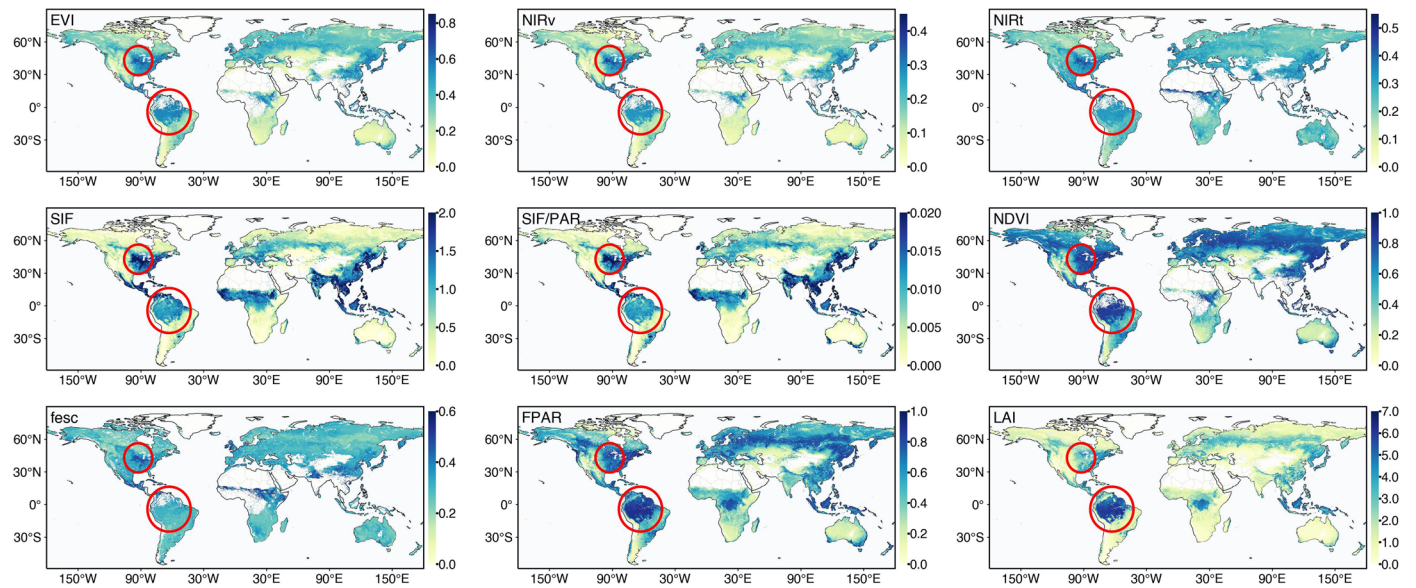
Peer review information *Nature Ecology & Evolution* thanks Anping Chen, Mathias Disney and Shangrong Lin for their contribution to the peer review of this work.

**Reprints and permissions information** is available at www.nature.com/reprints.

Extended Data Fig. 1 | The contrasting patterns between the Corn Belt (upper circle) and Amazon rainforest (lower circle) in August during 2001–2019 at global maps. The same as in Fig. 1, the MODIS EVI, NIRv and *fesc* were smaller over the Amazon rainforest than over the Corn Belt, while the MODIS LAI shows the opposite pattern. This effect is also found in the cropland in Northeast Asia, the rainforest in Southeast Asia, and the eastern forest region in North America near the Corn Belt with the same season and similar latitude.
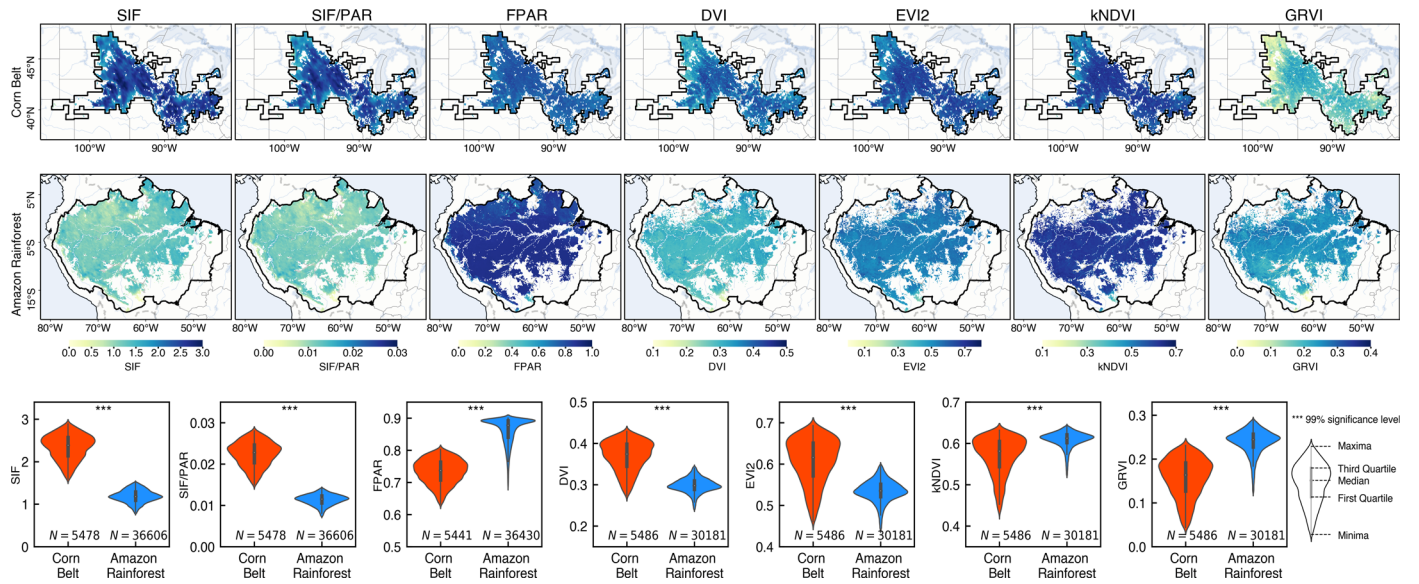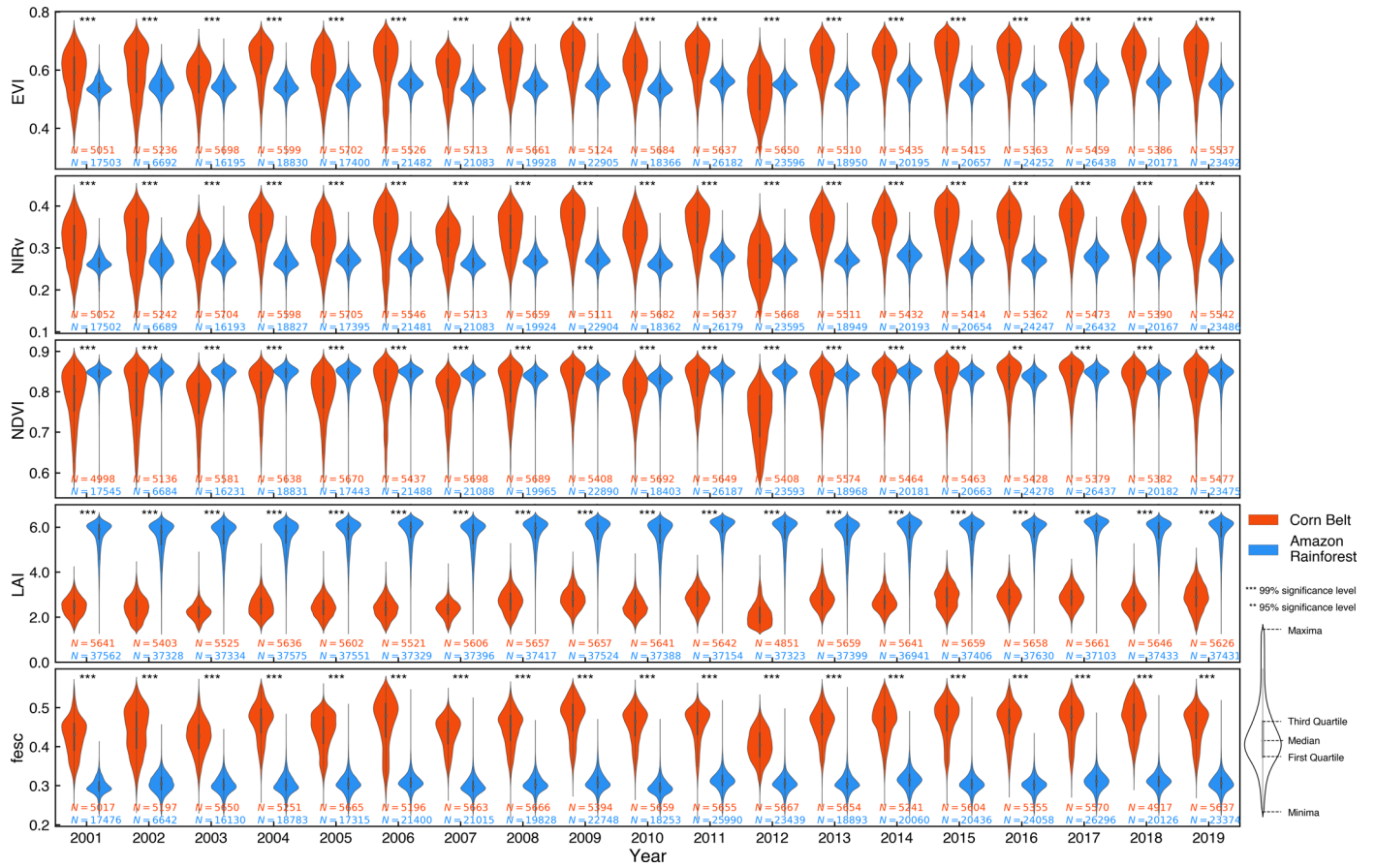
Extended Data Fig. 2 | Comparison of VIs, FPAR and SIF between the Corn Belt (upper panels) and Amazon rainforest (lower panels) in August during 2001–2019.
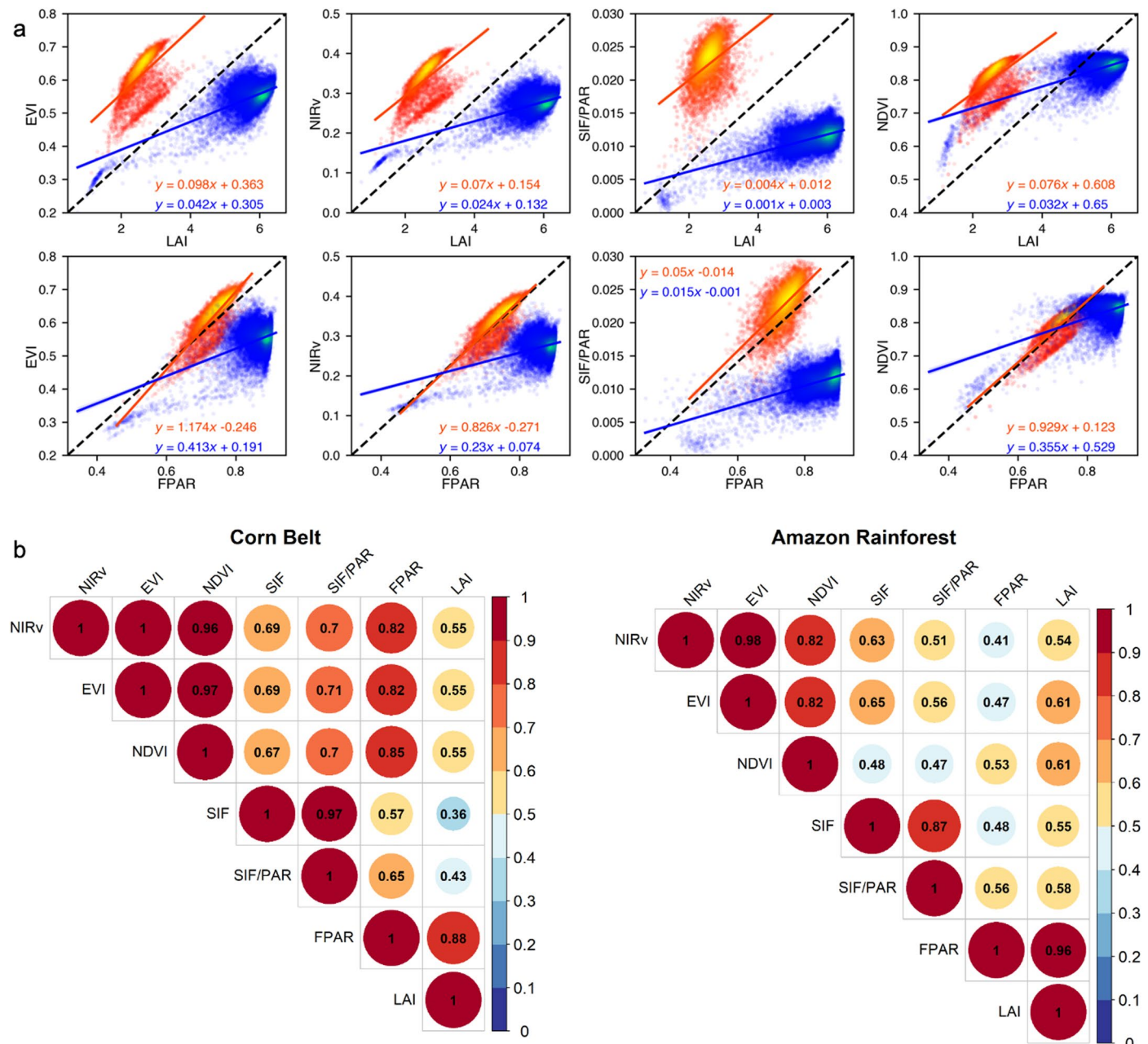
Extended Data Fig. 3 | The relationship among LAI, FPAR, SIF and VIs over the Corn Belt and Amazon rainforest. (a) The relationship between LAI or FPAR with EVI, NIRv, SIF/PAR and NDVI over the Corn Belt (in red) and Amazon rainforest (in blue) in August during 2001–2019. The linear slopes over the Corn Belt were at least twice as high as those over the Amazon rainforest. In each panel, the degree of point transparency represents the point density. **(b)** The correlation coefficient among LAI, FPAR, SIF and VIs over the Corn Belt and Amazon rainforest in August during 2001–2019. The relationship among VIs and SIF were much higher than they were compared to FPAR and LAI, especially over the Corn Belt.
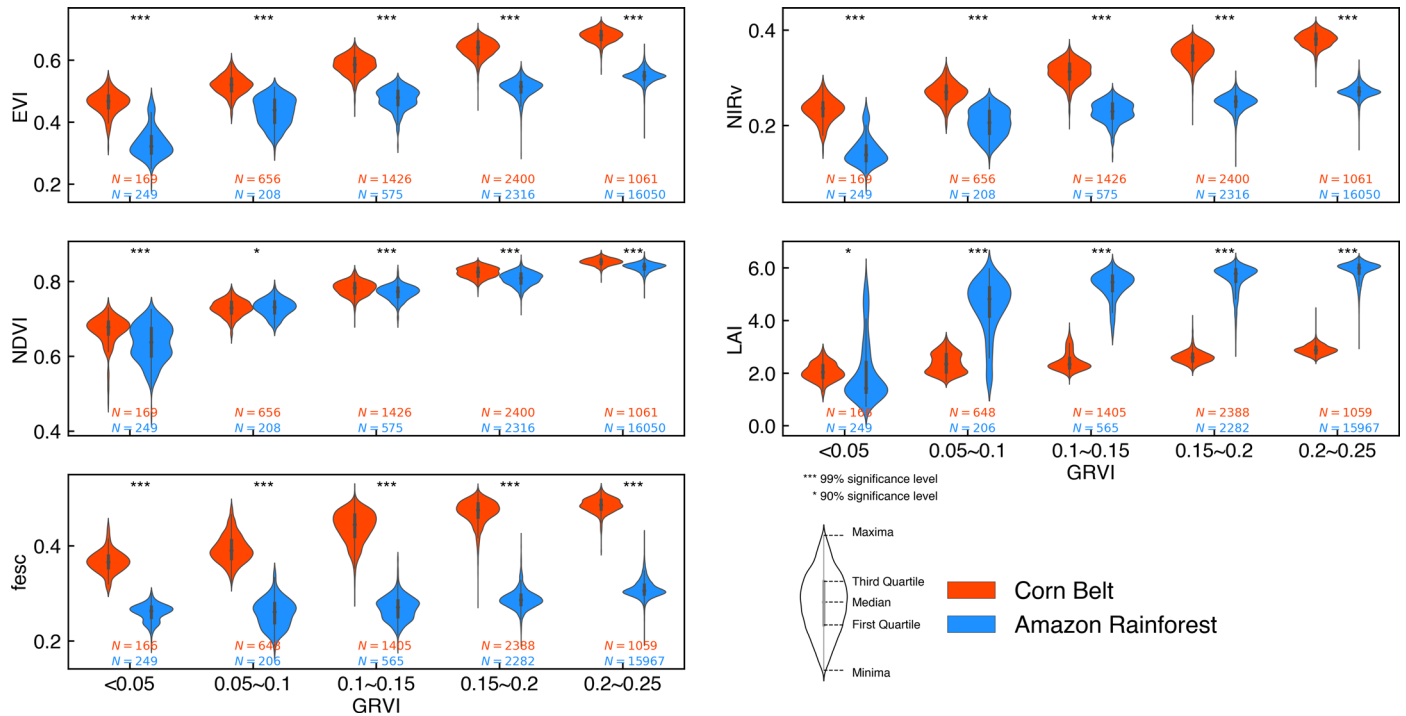
Extended Data Fig. 4 | Comparisons of VIs, LAI and *fesc* between the Corn Belt and Amazon rainforest in August of each year during 2001–2019.
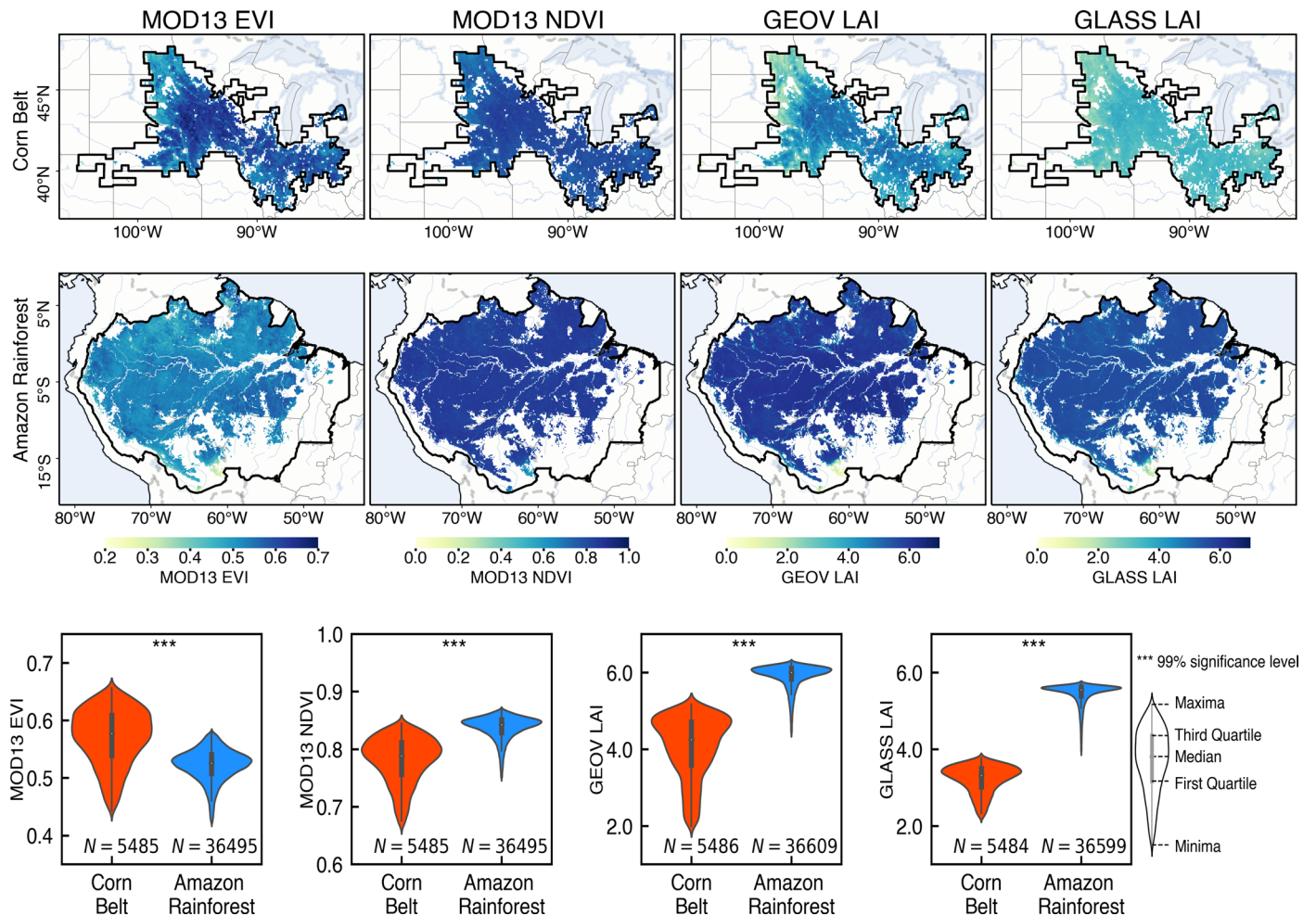
Extended Data Fig. 5 | The comparison of the Corn Belt (upper panels) and Amazon rainforest (lower panels) in August during the period of 2001–2019. Additional global VI and LAI products, including MOD13 NDVI/EVI, GEOV LAI and GLASS LAI, were used for the analysis in addition to the MCD43 NDVI/EVI and MODIS LAI shown in Fig. 1. Similar to Fig. 1, the EVI values are lower over the Amazon rainforest compared to the Corn Belt, while the LAI shows the opposite pattern, with larger values observed in the Amazon rainforest.

Extended Data Fig. 6 | Comparison of VIs, LAI and *fesc* between the Corn Belt and Amazon rainforest in August during 2001–2019 at different levels of GRVI, which was used as a proxy of canopy pigment pools.
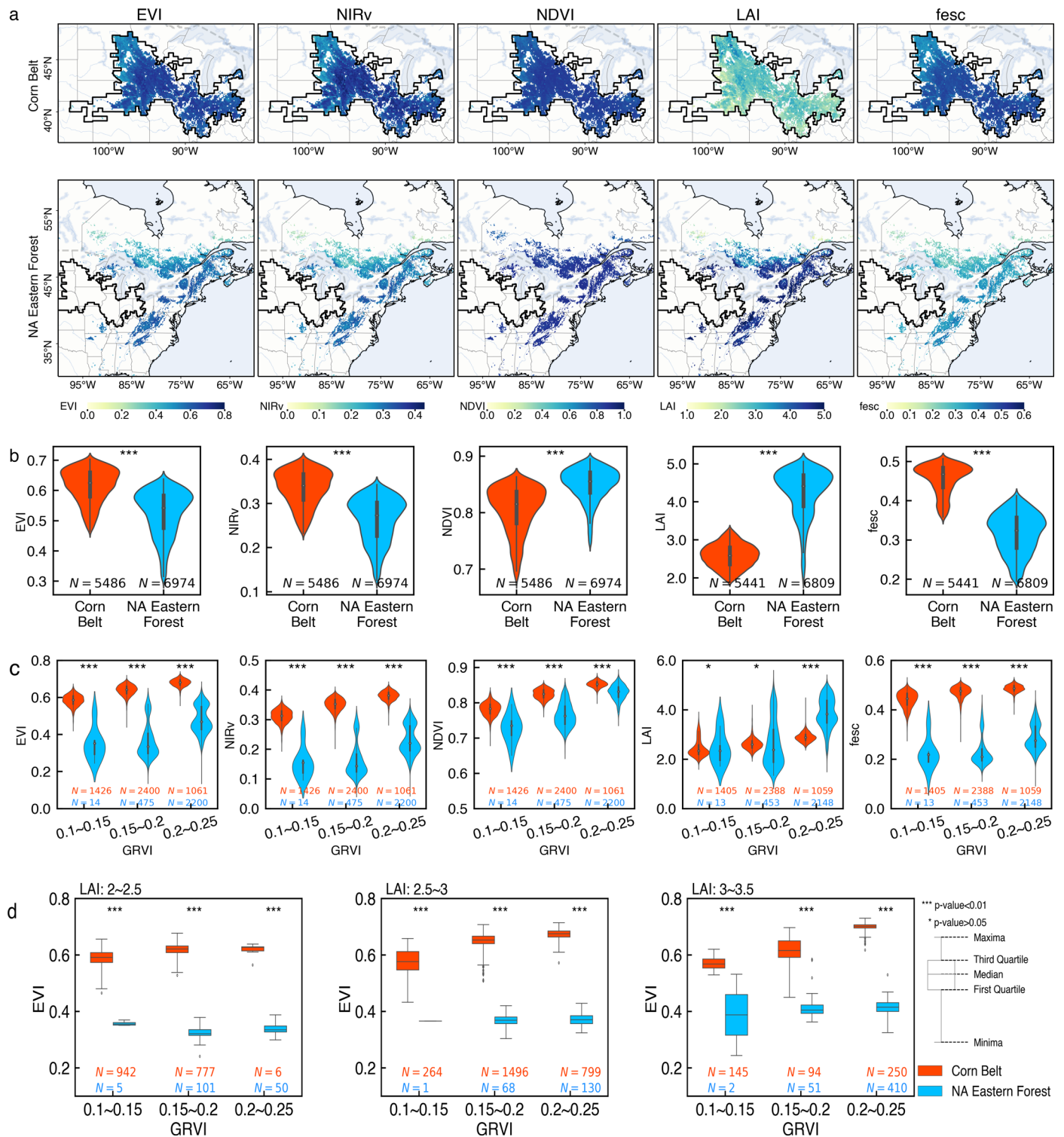
Extended Data Fig. 7 | Comparisons of VIs, LAI and *fesc* between the US Corn Belt (upper panels in a) and a nearby forest region in the Northeastern North America (NA, lower panels in a) in August during 2001–2019. (b) The MODIS EVI, NIRv and *fesc* were lower over the forest region compared to the Corn Belt, due to the stronger shadows in view. In contrast, the MODIS LAI was higher in the forest region than in the Corn Belt. The corresponding violin plots display the quartile and mean of the target variables, and as well as their distributions. **(c)** Comparison of VIs, LAI and *fesc* between the Corn Belt and the nearby forest region in North America in August during 2001–2019 at different levels of GRVI, which was used as a proxy of canopy pigment pools. **(d)** Comparison of EVI between the Corn Belt and the nearby forest region in North America in August during 2001–2019 at different levels of GRVI and LAI.
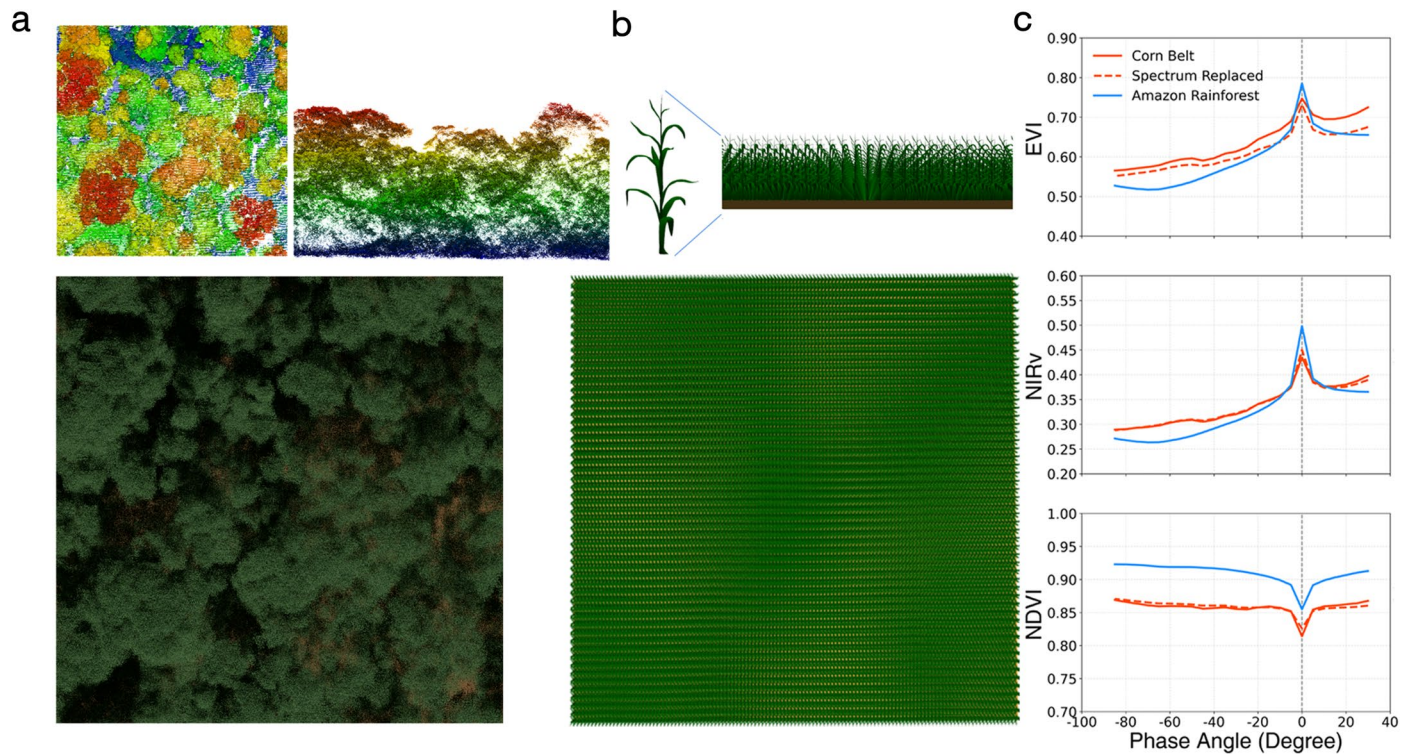
Extended Data Fig. 8 | The canopy structure reconstructed by the 3D ray-tracing model over the Amazon rainforest (a, 100 m × 100 m) and the corn field (b, 50 m × 50 m). The Amazon rainforest structure was extracted by the LiDAR data acquired over a site located at (E 54.99, S 3.37) in 2018[22]. Detailed input soil-leaf-canopy parameters were as in Supplementary Table 1. Multi-angular EVI, NIRv and NDVI simulations by the 3D ray-tracing model over the Corn Belt and Amazon rainforest **(c)** had close values at the hotspot direction (phase angle = 0 when the solar and sensor directions coincide), while EVI and NIRv were always much higher over the Corn Belt than the Amazon rainforest at the off-hotspot directions (phase angle > 0, for example, at nadir view but the solar zenith angle is 45° for the standard MAIAC surface reflectance product). The phase angle in **(c)** is the angle between the solar and sensor directions. The 'Spectrum Replaced' represents the simulation of the corn field while the soil-leaf spectrum was replaced by the spectrum of the Amazon rainforest **(c)**.
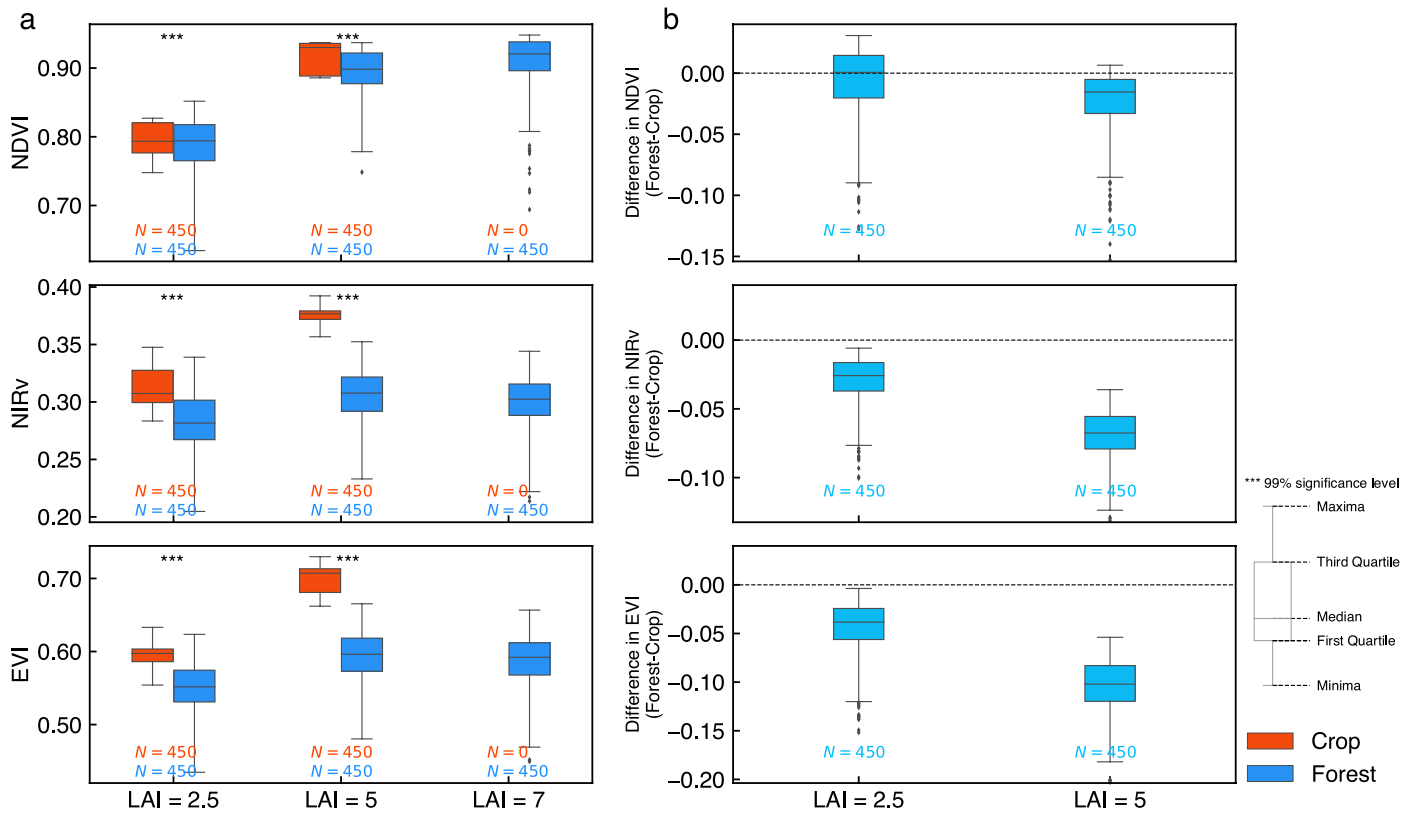
Extended Data Fig. 9 | Sensitivity analysis by the LESS 3D ray-tracing model simulations of forest and crops with varied parameters in Supplementary Table 2, especially under the control of the same LAI. (a) The separate simulated VIs of forest and crops. (b) The differences of simulated VIs between forest and crops. The same as the contrast in Extended Data Fig. 7d, the EVI and NIRv under the control of similar LAI (2.5 or 5) were smaller over forest than crops, especially when the LAI was relatively large at 5.
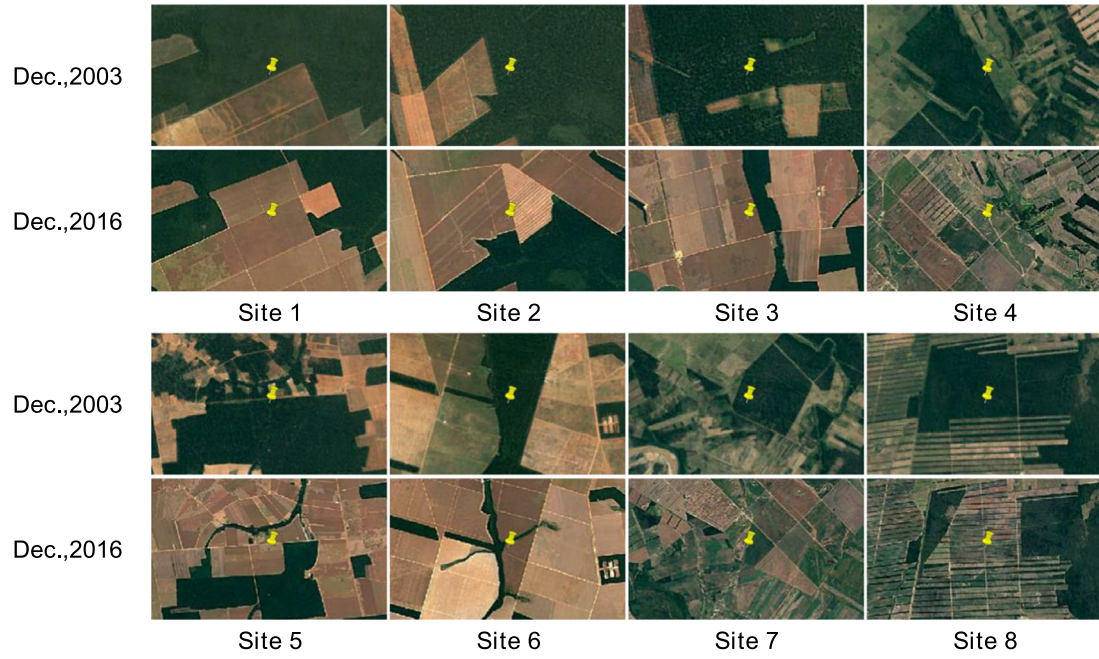
Extended Data Fig. 10 | The eight deforestation locations in Fig. 4a with the land cover change from forest to crops within 2005–2015 over Amazon rainforest.

nature portfolio

Corresponding author(s): Min Chen; Yelu Zeng; Dalei Hao

Last updated by author(s): Jul 10, 2023

Reporting Summary

Nature Portfolio wishes to improve the reproducibility of the work that we publish. This form provides structure for consistency and transparency in reporting. For further information on Nature Portfolio policies, see our Editorial Policies and the Editorial Policy Checklist.

Statistics

For all statistical analyses, confirm that the following items are present in the figure legend, table legend, main text, or Methods section.

n/a	Confirmed	
☐	☒	The exact sample size (*n*) for each experimental group/condition, given as a discrete number and unit of measurement
☒	☐	A statement on whether measurements were taken from distinct samples or whether the same sample was measured repeatedly
☐	☒	The statistical test(s) used AND whether they are one- or two-sided *Only common tests should be described solely by name; describe more complex techniques in the Methods section.*
☐	☒	A description of all covariates tested
☐	☒	A description of any assumptions or corrections, such as tests of normality and adjustment for multiple comparisons
☐	☒	A full description of the statistical parameters including central tendency (e.g. means) or other basic estimates (e.g. regression coefficient) AND variation (e.g. standard deviation) or associated estimates of uncertainty (e.g. confidence intervals)
☐	☒	For null hypothesis testing, the test statistic (e.g. *F*, *t*, *r*) with confidence intervals, effect sizes, degrees of freedom and *P* value noted *Give P values as exact values whenever suitable.*
☒	☐	For Bayesian analysis, information on the choice of priors and Markov chain Monte Carlo settings
☒	☐	For hierarchical and complex designs, identification of the appropriate level for tests and full reporting of outcomes
☒	☐	Estimates of effect sizes (e.g. Cohen's *d*, Pearson's *r*), indicating how they were calculated

Our web collection on statistics for biologists contains articles on many of the points above.

Software and code

Policy information about availability of computer code

Data collection	No software was used in the data collection.
Data analysis	Code used to generate figures and results is available through Figshare at https://doi.org/10.6084/m9.figshare.23677260.v1. The freely accessible platform Google Earth Engine (https://earthengine.google.com/platform/) was used for the MODIS data processing, and the LESS model (http://lessrt.org/) was used for the LiDAR dataset processing and 3D ray-tracing model simulations.

For manuscripts utilizing custom algorithms or software that are central to the research but not yet described in published literature, software must be made available to editors and reviewers. We strongly encourage code deposition in a community repository (e.g. GitHub). See the Nature Portfolio guidelines for submitting code & software for further information.

Data

Policy information about availability of data

All manuscripts must include a data availability statement. This statement should provide the following information, where applicable:
- Accession codes, unique identifiers, or web links for publicly available datasets
- A description of any restrictions on data availability
- For clinical datasets or third party data, please ensure that the statement adheres to our policy

The data are available through Figshare at https://doi.org/10.6084/m9.figshare.23677407.v1

Research involving human participants, their data, or biological material

Policy information about studies with human participants or human data. See also policy information about sex, gender (identity/presentation), and sexual orientation and race, ethnicity and racism.

Reporting on sex and gender	N/A
Reporting on race, ethnicity, or other socially relevant groupings	N/A
Population characteristics	N/A
Recruitment	N/A
Ethics oversight	N/A

Note that full information on the approval of the study protocol must also be provided in the manuscript.

Field-specific reporting

Please select the one below that is the best fit for your research. If you are not sure, read the appropriate sections before making your selection.

☐ Life sciences   ☐ Behavioural & social sciences   ☒ Ecological, evolutionary & environmental sciences

For a reference copy of the document with all sections, see nature.com/documents/nr-reporting-summary-flat.pdf

Ecological, evolutionary & environmental sciences study design

All studies must disclose on these points even when the disclosure is negative.

Study description	By synthesizing evidence from radiative transfer theory, multi-angular satellite observations, and state-of-the-art simulations, we reveal that macroscale shadows cast by complex forest structures lead to lower greenness measures compared to structurally simple and homogeneous crops.
Research sample	Global MODIS surface reflectance, VIs and LAI products during 2001-2019 with 500 m spatial resolution; Global TROPOMI SIF and EPIC PAR products during the period of 2018.03-2019.02; POLDER and MISR multi-angular surface reflectance products in the Corn Belt and Amazon rainforest; Earth Observing-1 Hyperion based canopy spectrum in the Corn Belt and Amazon rainforest; LiDAR dataset and 3D ray-tracing model simulations in the Amazon rainforest.
Sampling strategy	We used all available remote sensing samples except for those as described and justified in "Data exclusions".
Data collection	All MODIS datasets from 2001-2019 with 500 m spatial resolution were obtained from the Google Earth Engine (GEE) platform. The GEOV LAI product was acquired at https://land.copernicus.eu/global/products/lai The GLASS LAI product was acquired at http://www.glass.umd.edu/LAI/MODIS/0.1D/ The TROPOMI far-red daily SIF dataset with a spatial resolution of 7 km × 3.5 km at nadir was acquired at ftp://fluo.gps.caltech.edu/data/tropomi The LiDAR dataset was available through the Oak Ridge National Laboratory (ORNL) Distributed Active Archive Center (DAAC) at https://daac.ornl.gov/cgi-bin/dsviewer.pl?ds_id=1644 The site imageries at Tapajos and Mead1 were acquired at PhenoCam (https://phenocam.nau.edu/webcam/sites).
Timing and spatial scale	The daily MODIS MCD43A4 V6.1 NBAR, the 8-day MOD15A2H V6.1 LAI/FPAR, the 16-day MOD13A2 V6.1 EVI/NDVI, and the yearly MCD12Q1 V6.1 Land Cover Type products were acquired during 2001-2019 with 500 m spatial resolution. The data were aggregated to monthly temporally and 0.1° spatially. The TROPOMI far-red daily SIF dataset has a spatial resolution of 7 km × 3.5 km at nadir with the time period of 2018.03-2019.02. The POLDER observations were obtained between July and August 2008, with a spatial resolution of approximately 6.2 km. The MISR observations were collected during July and August 2017, with a spatial resolution of 1.1 km and a temporal resolution of 9 days. The Earth Observing-1 Hyperion image over the Corn Belt was acquired on Day of Year (DOY) 210 in 2014, while the Hyperion image over the Amazon rainforest was acquired on DOY 221 in 2002. The point cloud data was collected during LiDAR surveys at the Amazon rainforest in Brazil in 2018.
Data exclusions	We have used all relevant data according to the physical term definition and product standard quality. Our analyses excluded non-forest regions, such as savanna in the eastern part of the Amazon and grassland in the southern part of the Amazon, as identified by the MCD12 land cover product. We excluded all pixels in which non-vegetation types (such as snow/ice, water, barren land, and urban areas) comprised more than 50% of the total area. Additionally, we analyzed only homogeneous pixels composed of more than

80% forest or crop within vegetated areas. We only used snow-free MODIS NBAR and other data with good Quality Assurance (QA)/ Quality Control (QC) flags.

Reproducibility
We have shared the code in a publicly accessible repository.

Randomization
In the land conversion from forest to crops, we have explored both the eight randomly selected sites as examples, and the regional-scale with all the deforestation pixels.

Blinding
Blinding is not relevant because this work was not experimental in nature.

Did the study involve field work?   ☐ Yes   ☒ No

Reporting for specific materials, systems and methods

We require information from authors about some types of materials, experimental systems and methods used in many studies. Here, indicate whether each material, system or method listed is relevant to your study. If you are not sure if a list item applies to your research, read the appropriate section before selecting a response.

Materials & experimental systems

n/a	Involved in the study
☒ ☐	Antibodies
☒ ☐	Eukaryotic cell lines
☒ ☐	Palaeontology and archaeology
☒ ☐	Animals and other organisms
☒ ☐	Clinical data
☒ ☐	Dual use research of concern
☒ ☐	Plants

Methods

n/a	Involved in the study
☒ ☐	ChIP-seq
☒ ☐	Flow cytometry
☒ ☐	MRI-based neuroimaging